NANO LETTERS

pubs.acs.org/NanoLett

Letter

Super-Resolution Mapping of a Chemical Reaction Driven by Plasmonic Near-Fields

Ruben F. Hamans, Matteo Parente, and Andrea Baldi*

Cite This: *Nano Lett.* 2021, 21, 2149−2155

Read Online

ACCESS | Metrics & More | Article Recommendations | Supporting Information

ABSTRACT: Plasmonic nanoparticles have recently emerged as promising photocatalysts for light-driven chemical conversions. Their illumination results in the generation of highly energetic charge carriers, elevated surface temperatures, and enhanced electromagnetic fields. Distinguishing between these often-overlapping processes is of paramount importance for the rational design of future plasmonic photocatalysts. However, the study of plasmon-driven chemical reactions is typically performed at the ensemble level and, therefore, is limited by the intrinsic heterogeneity of the catalysts. Here, we report an in situ single-particle study of a fluorogenic chemical reaction driven solely by plasmonic near-fields. Using super-resolution fluorescence microscopy, we map the position of individual product molecules with an ∼30 nm spatial resolution and demonstrate a clear correlation between the electric field distribution around individual nanoparticles and their super-resolved catalytic activity maps. Our results can be extended to systems with more complex electric field distributions, thereby guiding the design of future advanced photocatalysts.

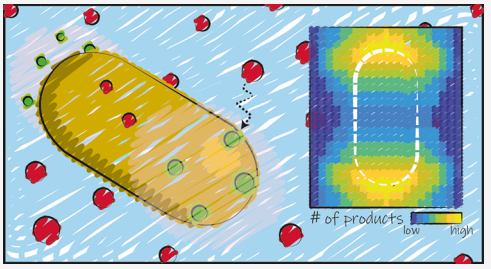

KEYWORDS: *plasmonics, photochemistry, near-fields, fluorogenic reactions, super-resolution microscopy*

INTRODUCTION

Localized surface plasmon resonances (LSPRs) arise from the coherent oscillation of free electrons upon illumination of metallic nanoparticles.[1] These resonances can enhance the rate of chemical reactions and change their potential energy landscape.[2−5] For example, LSPRs have been used to enhance the rate of NH_3 decomposition on copper−ruthenium nanoparticles[6] and to increase the selectivity of a CO_2 hydrogenation on rhodium nanocubes.[7] At least three mechanisms have been proposed to explain the observed enhancements: (i) the generation of nonequilibrium charge carriers driving redox reactions, (ii) photothermal nanoparticle heating inducing faster chemical turnover according to the Arrhenius equation, and (iii) focusing of light into nanoscale regions of high electromagnetic fields (near-fields) that accelerate photosensitive reactions.[8] All these mechanisms take place on ultrafast time scales and can contribute simultaneously to the enhancement of a chemical reaction, making them very difficult to disentangle experimentally.[8−10]

Recent studies have begun elucidating the mechanism underlying a wide range of plasmon-driven processes by carefully characterizing the rate of chemical reactions under different illumination parameters, while measuring the temperature inside the reactor.[6,11−14] These experiments are often performed at the ensemble level, resulting in measurements that are averaged over many particles. The photocatalytic properties of nanoparticles, however, are intrinsically heterogeneous due to the distribution in particle sizes and orientations with respect to the incoming light,[15,16] the heterogeneity of active sites,[17] and the dynamic restructuring of catalytic surfaces.[18−20] For this reason, in situ measurements of the catalytic activity of single nanoparticles with single-molecule accuracy and nanometer spatial resolution are necessary.[21−24] In this context, super-resolution fluorescence microscopy has emerged as an effective approach thanks to its ability to interrogate individual catalytic nanoparticles at the single-molecule level.[21] For example, super-resolution microscopy has been used to characterize chemical reactions that are accelerated by plasmonic hot charge carriers.[25,26] However, the efficiency of hot charge carrier extraction is typically very low due to the extremely short lifetimes.[27,28] Recently, several studies have proposed an alternative mechanism to explain the plasmon-driven catalysis enhancements, in which the plasmonic near-field induced direct optical excitations of adsorbate molecules.[29−32] To demonstrate this mechanism, which is not limited by fast electron−electron scattering and could therefore result in high conversion efficiencies, it is important to spatially correlate the photocatalytic activity of individual metal nanoparticles with their plasmonic near-fields.

Here, we utilize super-resolution microscopy to map the activation of a purely field-driven chemical reaction under in

Received: December 15, 2020
Revised: February 2, 2021
Published: February 19, 2021

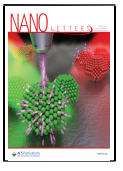

https://dx.doi.org/10.1021/acs.nanolett.0c04837
Nano Lett. 2021, 21, 2149−2155

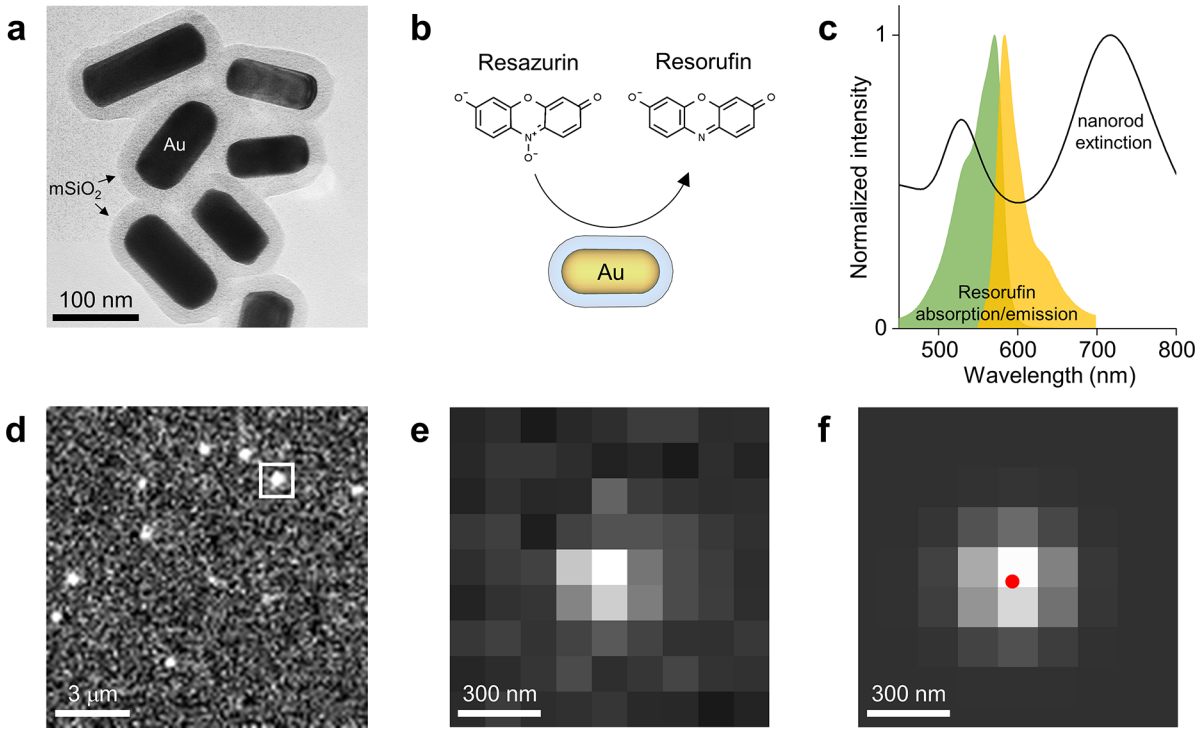

Figure 1. In situ super-resolution catalysis on individual gold nanorods. (a) Transmission electron microscopy image of the Au@$mSiO_2$ nanorods after ligand removal. (b) Illustration of the catalytic conversion of resazurin to resorufin. (c) Normalized extinction of a colloidal solution of Au@$mSiO_2$ nanorods after ligand removal (black line) and absorption (green) and emission (yellow) of the reaction product resorufin. (d) Example frame showing the fluorescence of resorufin molecules generated on several catalysts. The image displayed here is cropped from the total field-of-view of 133 × 133 μm^2. (e) Enlarged area denoted by the white box in (d), showing the emission of one resorufin molecule. (f) Two-dimensional Gaussian fit of panel (e). The resulting molecule position is denoted by the red dot.

situ conditions. In particular, we irradiate gold nanorods that catalyze the conversion of the nonfluorescent molecule resazurin (Rz) to its highly fluorescent reduced form resorufin (Rf).[33] The power dependence of the turnover rate and the spatial distribution of the catalytic events unequivocally indicate that the activation mechanism is solely due to the plasmonic near-fields.

RESULTS AND DISCUSSION

We first synthesize gold (Au) nanorods with a length of 118 ± 10 nm and a width of 54 ± 4 nm using a previously reported seed-mediated process (Figure S1).[16] These dimensions result in a longitudinal LSPR at 718 nm, which is spectrally separated from the emission of the reaction product resorufin and thereby minimizes mislocalization effects.[34−37] We then coat the nanorods with an ∼16 nm mesoporous SiO_2 ($mSiO_2$) shell using a previously reported growth method (Figure 1a and Figure S1).[38,39] The mesoporous shell with ∼2.5 nm pores[39] temporarily traps the reaction products and thereby facilitates their detection, which would otherwise be hindered by fast product desorption and fluorescence quenching on Au.[40] Interestingly, our Au@$mSiO_2$ nanorods show no catalytic activity in the dark, suggesting that the mesopores do not extend all the way to the metallic surface (Figure S2).

We dropcast the Au@$mSiO_2$ nanorods on a coverslip, resulting in an average interparticle spacing of ∼6 μm, which allows each rod to be resolved spatially in the microscope. The coverslip is then built into a flow cell supplying a continuous flow of 200 nM resazurin, and the assembly is mounted on an inverted fluorescence microscope (Figure S3).

At the beginning of each experiment, we first take a transmitted white light image of the sample. We fit all local transmission minima to two-dimensional Gaussians and thereby localize all nanoparticles with an ∼6 nm precision (Figure S4).[41−43] We then irradiate an area of the sample of ∼100 × 100 μm^2 with a 532 nm continuous-wave (CW) laser in a total internal reflection (TIRF) configuration (Figure S3). This laser wavelength simultaneously excites the reaction product resorufin and the transverse plasmon resonance of the nanorods (Figures 1b,c). The nanorod photoluminescence closely follows its longitudinal plasmon resonance (λ = 718 nm),[44] which is outside the spectral range of the emission filter. Therefore, in our experimental configuration, we do not need to perform a background subtraction to remove the nanorod photoluminescence, and we only observe stochastic bursts of fluorescence corresponding to the generation of resorufin molecules.[33] Similar to the localization procedure for the nanoparticles, we localize these bursts (Figures 1d,e) by fitting them to two-dimensional Gaussians (Figure 1f), resulting in a localization precision of ∼24 nm (Figure S5). Combined with the error in the nanoparticle locations, the overall localization precision of the experiment is ∼30 nm.

Resazurin (Rz) can be converted to resorufin (Rf) via two different mechanisms:[45] (i) a reductive deoxygenation catalyzed by Au, which requires the presence of hydroxylamine (NH_2OH) as a reducing agent[21]

$$2Rz + NH_2OH + OH^- \xrightarrow{Au} 2Rf + NO_2^- + 2H_2O \quad (1)$$

or (ii) a photodriven disproportionation[33]

https://dx.doi.org/10.1021/acs.nanolett.0c04837
Nano Lett. 2021, 21, 2149−2155

$$3\mathrm{Rz} + \mathrm{H_2O} \xrightarrow{\hbar\omega} \mathrm{Rf} + 2\mathrm{Rz}\cdot + 2\mathrm{OH}^- \quad (2)$$

where Rz· indicates an oxidized radical of resazurin.

The first mechanism occurs under dark conditions, but it can be enhanced by exciting the plasmon resonance of the catalysts.[25] The second mechanism does not occur under dark conditions and does not strictly require a catalytic surface but exhibits faster dynamics in the presence of Pd or Au nanoparticles.[33] These two reaction pathways are characterized by different dependencies of the turnover rate (number of detected products per catalyst per second) on the laser power. The reductive deoxygenation in eq 1 shows a quadratic power dependence, which has been attributed to the presence of two photoexcited species on the nanoparticle surface.[25] In the absence of a catalytic surface, the photodriven disproportionation in eq 2 also shows a quadratic dependence, as each reaction involves two photoexcited resazurin molecules.[33] In the presence of a catalytic surface, however, the turnover rate of the second mechanism increases linearly, suggesting a different reaction pathway involving a single photoexcited resazurin molecule.[33]

To discern between these reaction pathways, we measure the turnover rate as a function of laser power both in the absence and presence of the reducing agent NH_2OH (Figure 2a). To exclude fluorescent impurities, we only consider events detected within 100 nm of a Au@mSiO$_2$ catalyst. The observed trend of the turnover rate on the laser power does not strongly depend on this distance threshold (Figure S6). Every 10 000 frames (corresponding to ~20 min) we reduce the laser power in steps of 20 mW from 200 to 100 mW, and then, to check the reversibility of the laser power dependence, we increase the power back to 200 mW as the final step (right y-axis in Figure 2a). We observe a decrease in turnover rate with decreasing laser power, which is almost fully reversible (Figure 2a). We also find that this decrease in turnover rate is not due to a decrease in the detectability of the reaction products, as the amount of events that are not localized on a catalyst, such as fluorescent bursts from impurities or reaction products that readsorb on the glass coverslip, does not vary with laser power (Figure S7). As our mSiO$_2$ shells are both thin and porous, we attribute the incomplete recovery of the initial catalytic activity to the partial dissolution of SiO_2 in water,[39,46] which decreases the ability of the shell to temporarily trap the reaction products.

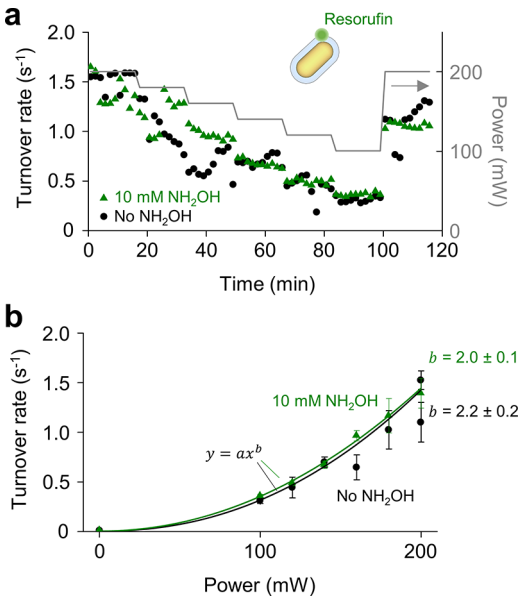

Figure 2. Kinetics of the Rz to Rf conversion. (a) Mean turnover rate as a function of time in the absence (black circles) and presence (green triangles) of 10 mM NH_2OH. Every point is an average over 1000 frames and 485 particles (black circles) or 331 particles (green triangles). (b) Turnover rate as a function of laser power in the absence (black circles) and presence (green triangles) of 10 mM NH_2OH. Each point is the average of 10 points in panel (a). Error bars are standard deviations. Solid lines are a fit to $y = ax^b$, where y is the turnover rate, x is the laser power, and a and b are fitting parameters.

Plotting the turnover rate as a function of laser power and fitting the results to a power law ($y = ax^b$) reveals a quadratic dependence both in the presence and absence of 10 mM NH_2OH (Figure 2b). Intermediate NH_2OH concentrations also show no influence on the turnover rate (Figure S8). Therefore, we can conclude that our catalysts are inactive for the reductive deoxygenation, as the presence of NH_2OH does not alter the reaction kinetics. Furthermore, the catalysts are also inactive for the photodriven disproportionation mediated by a catalytic surface, as we observe a quadratic rather than a linear dependence of the turnover rate on laser power. The quadratic power dependence in the absence of NH_2OH indicates that, in our system, the conversion of resazurin to resorufin is not mediated by an electron transfer with Au. Instead, we exploit the capability of Au nanoparticles to focus light into sub-wavelength volumes (near-fields) and thereby accelerate photodriven reactions in the vicinity of their surface.

Since in our system no electron transfer takes place between Au and resazurin, we can rule out any contribution from nonequilibrium charge carriers generated through plasmon excitation. We further verify this statement by simultaneously exciting the longitudinal plasmon resonance of the Au@mSiO$_2$ nanorods using a 730 nm CW laser. While at this energy resazurin is not photoexcited (Figure S9), the charge carriers generated by absorption in Au have enough energy to occupy the lowest unoccupied molecular orbital of resazurin.[33] However, we observe no change in the kinetics of the reaction when comparing the reaction rate with or without the excitation of the longitudinal resonance of the rods (Figure S9). Furthermore, because of the low power density and large interparticle spacing used in our study, localized and collective photothermal contributions can also safely be ruled out (Figure S10), thereby leaving the plasmonic near-fields as the sole contributor to the resazurin-to-resorufin conversion.

The observation that, in our system, the conversion of resazurin to resorufin is driven by the plasmonic near-fields suggests that a correlation should exist between the spatial distribution of the electric field around the nanorods and the regions where we observe a high catalytic activity. We therefore first simulate the optical response of our nanorods under 532 nm irradiation using a finite-difference time-domain (FDTD) method. We simulate a Au@mSiO$_2$ nanorod on a glass coverslip, and we inject a p-polarized field through the glass coverslip (Figure 3a and Figure S11). The long axis of the rod is pointing along the x-axis (Figure 3a), which we will refer to as p-oriented, or along the y-axis, which we will refer to as s-oriented. We monitor the absorption and scattering cross sections, σ_{abs} and σ_{sca}, and the total electric field intensity inside and outside the rod for various injection angles of the source. For a source angle of 0°, which corresponds to an injection

https://dx.doi.org/10.1021/acs.nanolett.0c04837
Nano Lett. 2021, 21, 2149−2155

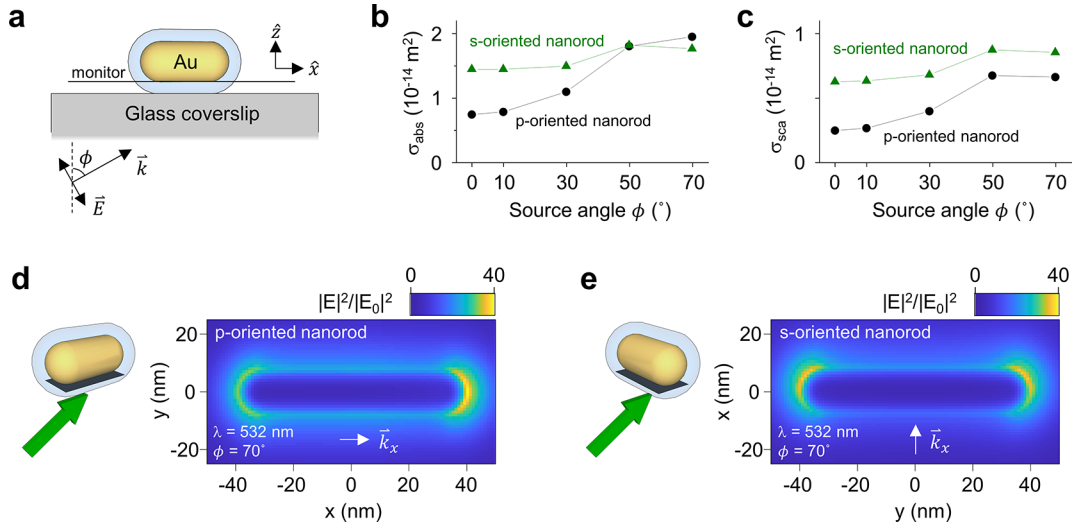

Figure 3. FDTD simulations on Au@mSiO$_2$ nanorods. (a) Illustration of the simulation. A p-polarized field $\vec{E}$ with wavevector $\vec{k}$ is injected on a Au@mSiO$_2$ nanorod on a glass coverslip. The source angle ϕ is defined as the angle between $\vec{k}$ and $\hat{z}$. The electric field is monitored at the bottom of the nanorod. (b, c) Absorption (b) and scattering (c) cross sections at 532 nm as a function of source angle. The nanorod is p-oriented (black circles), as in panel (a), or s-oriented (green triangles). The critical angle for TIRF is 61°. (d, e) Electric field intensity $|E|^2$ normalized to the incident field intensity $|E_0|^2$ at 532 nm monitored at the bottom of the Au nanorods for a source angle of 70°. The nanorod is p-oriented (d), as in panel (a), or s-oriented (e).

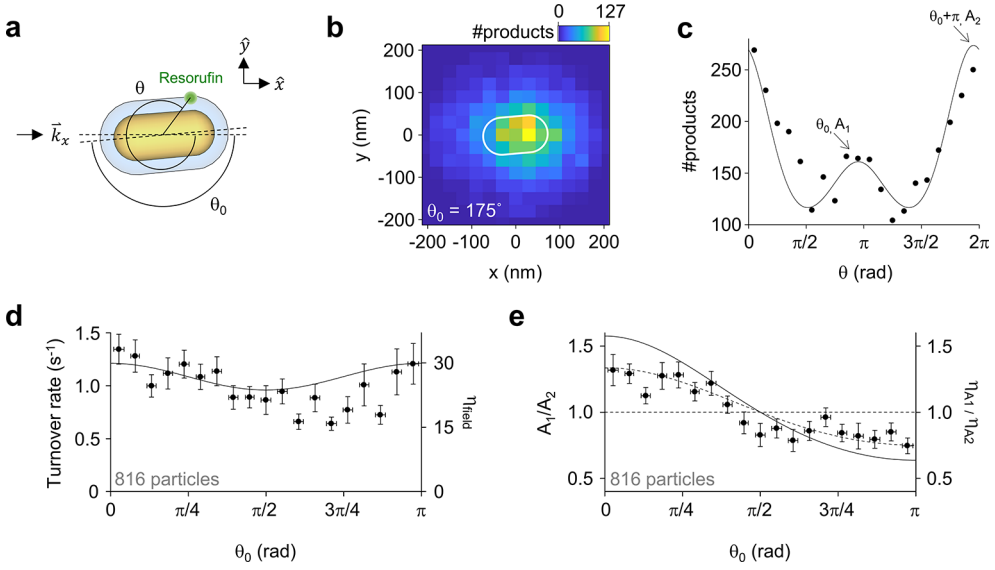

Figure 4. Analyzing catalysis maps as a function of particle orientation. (a) Illustration of the definition of the angle θ and the particle orientation θ_0. The x component of the wavevector $\vec{k}$ is also illustrated. (b, c) Two-dimensional histogram (b) and angular distribution (c) of the products detected within 200 nm of a single Au nanorod. The bin sizes are 30 × 30 nm^2 (b) and $\pi/10$ (c). Panel (b) also contains a white outline depicting the fitted position and orientation of the Au@mSiO$_2$ nanorod catalyst. The orientation θ_0 is extracted from the fit in panel (c). (d) Mean turnover rate as a function of particle orientation (circles) and the simulated electric field enhancement (line), as defined in eq 3. (e) Mean ratio between the peaks in the angular distribution (circles) and the ratio between the simulated electric field enhancements on the two tips (lines) as a function of particle orientation. In the simulation we consider the whole mSiO$_2$ shell (solid line) or the outer 5 nm of the shell (dashed line). In (d, e) the data from both the experiments with and without NH_2OH are used, resulting in a total of 816 particles. The points correspond to a bin with a width of $\pi/19$, the x error bars are standard deviations, and the y error bars are standard errors in the mean.

normal to the coverslip, the cross sections at 532 nm are higher for the s-oriented rod (Figure 3b,c). This behavior is expected, as the 532 nm illumination overlaps with the transverse resonance of Au nanorods (Figure S11), which is preferentially excited when the polarization of the field is perpendicular to the long axis of the rod. However, as the source angle increases, a second transverse resonance with charges oscillating along the z-axis is excited.[47] As the rod is always oriented in the x,y plane, this resonance is excited independently of the rod orientation when the source is off-axis, resulting in the cross sections for p-oriented and s-oriented rods becoming increasingly similar as the source angle increases (Figure 3b,c).

As the TIRF illumination corresponds to an excitation at very high angles (between 61° and 74° in our experimental geometry), the absorption and scattering cross sections of a nanorod do not depend strongly on the in-plane particle orientation. However, the spatial distribution of the electric

https://dx.doi.org/10.1021/acs.nanolett.0c04837
Nano Lett. 2021, 21, 2149−2155

field does show distinguishing features. We observe electric field hot spots at the bottom of the nanorod (Figure 3d,e) and a relatively weak field enhancement at the nanorod center (Figure S11). For the p-oriented rod the field intensity is ~1.3× higher on the tip away from the incident light than on the tip facing the source (Figure 3d). We do not observe this difference for the s-oriented rod, as this orientation is perpendicular to the propagation direction of the field, which leads to an identical distribution of enhanced fields at the opposing ends of the nanorod (Figure 3e).

The above observations suggest that, for varying in-plane orientations, we expect similar turnover rates but different spatial distributions of catalytic events. Since the dimensions of our catalysts are only a few times larger than our resorufin product localization precision, a quantitative comparison between the simulated electric field and the catalysis maps is challenging. Additionally, because of a partial spectral overlap of the nanorod extinction with the resorufin emission, the latter can couple to the nanorod, resulting in the apparent position of the molecule being "pulled" toward the nanorod center (Figure S12).[34,35] However, despite these limitations, our spatial resolution is sufficient to discriminate between the catalytic activity of the two tips of the rods. Therefore, to correlate the observed catalytic activity to the simulated electric field, we look at the in-plane angular distribution of catalytic events.

For each nanorod, we define the positions of the catalytic events relative to the position of the rod, which is known from the transmitted white light image. We then assign an angle θ to each catalytic event, defined as the angle between the position of the event and the x-axis (Figure 4a).

Instead of plotting the detected products on a single particle as a two-dimensional map (Figure 4b), this definition of θ allows us to plot the detected products as an angular distribution (dots in Figure 4c). For these angular distributions we use a bin size of $\pi/10$, which is commensurate with the typical error in θ (Figure S13). We then fit this distribution to a function given by the sum of two Gaussian peaks, corresponding to the two tips of the nanorod. The first peak models the catalytic activity of the front tip with a negative y-coordinate and is characterized by an amplitude A_1 and an in-plane orientation of θ_0. The second peak, corresponding to the back tip with a positive y-coordinate, has an amplitude A_2 and an in-plane orientation of $\theta_0 + \pi$ (Figure S14). Fitting the angular distribution of catalytic events allows us to extract the particle orientation θ_0 and the reactivities of the two nanorod tips, A_1 and A_2 (Figure 4c).

When $\theta_0 \approx 0$, the particle is p-oriented. In this orientation A_1 corresponds to the reactivity of the tip away from the incident light, where the field is higher than on the tip facing the source (Figure 3d), and therefore we expect $A_1 > A_2$. When $\theta_0 \approx \pi/2$, the particle is s-oriented. In this orientation the field enhancement on the two tips is equal (Figure 3e), and we expect $A_1 \approx A_2$. Lastly, when $\theta_0 \approx \pi$, the particle is again p-oriented. However, A_1 now corresponds to the reactivity of the tip facing the source, and we expect $A_1 < A_2$. The example shown in Figure 4a–c corresponds to a particle with $\theta_0 = 175°$ and for which A_1 is therefore smaller than A_2, as shown by the clear peak intensity difference in Figure 4c. Other examples of nanorods with different in-plane orientations can be found in Figure S15.

In Figure 4d, we bin together particles with similar in-plane orientations and plot the measured turnover rates as a function of θ_0, where the bin size is commensurate with the typical fitting error in θ_0 (Figure S14). Since the turnover rate scales quadratically with the electric field intensity (Figure 2b), we compare these values to the square of the average simulated electric field intensity outside the nanoparticle. We calculate this value η_{field} by integrating over all mesh cells outside the particle, but within the $mSiO_2$ shell

$$\eta_{\text{field}} = \frac{1}{V}\iiint_{r<16\text{nm}} \frac{|E|^4}{|E_0|^4}\mathrm{d}V \tag{3}$$

where V is the integrated volume, r is the distance from a mesh cell outside of the nanoparticle to the particle surface, E is the electric field, and E_0 is the incident field.

We find that both the turnover rate and the average field enhancement show only a weak dependence on the particle orientation (Figure 4d), as also expected from the similar scattering cross sections of p-oriented and s-oriented nanorods at the experimental illumination angle (Figure 3c). Interestingly, however, we find a clear angular dependence of the peak ratio A_1/A_2 on θ_0 (Figure 4e).

We compare this value to the ratio between the simulated field enhancement η_{A1} in the half-space occupied by the tip corresponding to A_1 and the field enhancement η_{A2} in the half-space occupied by the tip corresponding to A_2.

The measured ratio between the photocatalytic activity of the two tips of the nanorods (A_1/A_2) matches qualitatively with the simulated ratio between the electric field intensity enhancements on the two tips (η_{A1}/η_{A2}), as both show a transition from values greater than 1 for in-plane orientations $\theta_0 < \pi/2$ to values less than 1 for $\theta_0 > \pi/2$ (Figure 4e). Interestingly, if we assume that all molecules are detected within the outer 5 nm of the $mSiO_2$ shell, we obtain a quantitative agreement (dashed line in Figure 4e). This assumption is justified by the fact that the mesopores likely do not extend all the way to the metallic surface, as our catalysts are inactive in the dark, and by the fact that fluorescence quenching can occur for molecules generated in the vicinity of the Au surface. Such a quantitative agreement does not take into account the potential mislocalization of the resazurin emission, due to coupling to the nanorod plasmon resonance.[34−37] Although these effects are likely to be small (Figure S12), a proper quantitative agreement should rely on exact calculations of these effects for our experimental particle-molecule geometries.

CONCLUSION

In summary, we use super-resolution fluorescence microscopy for the in situ study of a plasmon-driven chemical reaction. We begin by identifying the reaction mechanism as a photodriven disproportionation by measuring the photocatalytic turnover rate at the single-molecule level for various illumination intensities and reducing agent concentrations. We then use single-molecule localization to show a clear correlation between the simulated electric field distribution and the super-resolution catalysis maps. Our photochemical approach to map scattered near-fields in situ and with a subparticle spatial resolution can be extended to systems with different chemical compositions and complex field distributions and can thereby guide the design of future advanced materials for photocatalysis, biomolecule sensing, and photonic devices.

https://dx.doi.org/10.1021/acs.nanolett.0c04837
Nano Lett. 2021, 21, 2149−2155

■ ASSOCIATED CONTENT

Supporting Information

The Supporting Information is available free of charge at https://pubs.acs.org/doi/10.1021/acs.nanolett.0c04837.

Synthesis of the Au@mSiO$_2$ catalysts; the Au@mSiO$_2$ nanorods show no catalytic activity in the dark; microscopy setup; localization of the catalysts in the microscope; localization precision of the resorfin molecules; the observed power dependencies do not strongly depend on the distance threshold; the observed power dependencies are not due to a change in product detectability; NH_2OH does not influence the reaction kinetics; independently exciting the LSPR of the Au@mSiO$_2$ nanorods does not alter the reaction kinetics; photothermal contributions are negligible; design of the FDTD simulations, FDTD spectra at normal incidence, and electric fields monitored at the nanorod center; mislocalization effects; error in the angle θ of a catalytic event; fitting function, θ_0 histogram, and fitting error in θ_0; single-particle catalysis maps and angular distributions (PDF)

■ AUTHOR INFORMATION

Corresponding Author

Andrea Baldi − *Dutch Institute for Fundamental Energy Research, 5612 AJ Eindhoven, The Netherlands; Department of Physics and Astronomy, Vrije Universiteit Amsterdam, 1081 HV Amsterdam, The Netherlands;* orcid.org/0000-0001-9044-9378; Email: a.baldi@vu.nl

Authors

Ruben F. Hamans − *Dutch Institute for Fundamental Energy Research, 5612 AJ Eindhoven, The Netherlands; Department of Physics and Astronomy, Vrije Universiteit Amsterdam, 1081 HV Amsterdam, The Netherlands*

Matteo Parente − *Dutch Institute for Fundamental Energy Research, 5612 AJ Eindhoven, The Netherlands*

Complete contact information is available at: https://pubs.acs.org/10.1021/acs.nanolett.0c04837

Author Contributions

All authors conceived the project; R.F.H. and M.P. performed the experiments; R.F.H. analyzed the data and performed the FDTD simulations; A.B. supervised the project; all authors contributed to writing the paper.

Notes

The authors declare no competing financial interest.

■ ACKNOWLEDGMENTS

The authors acknowledge R. Kamarudheen and G. Kumari for useful discussions, F. Nugroho for giving feedback on the manuscript and for the TOC graphic, and J. Reinders and G. Aalbers for taking transmission electron microscopy images. R.F.H. and A.B. acknowledge support from The Netherlands Organisation for Scientific Research through the NWO Vidi Award 680-47-550.

■ REFERENCES

(1) Bohren, C. F.; Huffman, D. R. *Absorption and Scattering of Light by Small Particles;* John Wiley & Sons: New York, 2008.

(2) Linic, S.; Aslam, U.; Boerigter, C.; Morabito, M. Photochemical Transformations on Plasmonic Metal Nanoparticles. *Nat. Mater.* **2015**, *14*, 567−576.

(3) Zhang, Y.; He, S.; Guo, W.; Hu, Y.; Huang, J.; Mulcahy, J. R.; Wei, W. D. Surface-plasmon-driven Hot Electron Photochemistry. *Chem. Rev.* **2018**, *118*, 2927−2954.

(4) Aslam, U.; Rao, V. G.; Chavez, S.; Linic, S. Catalytic Conversion of Solar to Chemical Energy on Plasmonic Metal Nanostructures. *Nature Catalysis* **2018**, *1*, 656−665.

(5) Zhang, Z.; Zhang, C.; Zheng, H.; Xu, H. Plasmon-driven Catalysis on Molecules and Nanomaterials. *Acc. Chem. Res.* **2019**, *52*, 2506−2515.

(6) Zhou, L.; Swearer, D. F.; Zhang, C.; Robatjazi, H.; Zhao, H.; Henderson, L.; Dong, L.; Christopher, P.; Carter, E. A.; Nordlander, P.; et al. Quantifying Hot Carrier and Thermal Contributions in Plasmonic Photocatalysis. *Science* **2018**, *362*, 69−72.

(7) Zhang, X.; Li, X.; Zhang, D.; Su, N. Q.; Yang, W.; Everitt, H. O.; Liu, J. Product Selectivity in Plasmonic Photocatalysis for Carbon Dioxide Hydrogenation. *Nat. Commun.* **2017**, *8*, 1−9.

(8) Brongersma, M. L.; Halas, N. J.; Nordlander, P. Plasmon-induced Hot Carrier Science and Technology. *Nat. Nanotechnol.* **2015**, *10*, 25.

(9) Aizpurua, J.; Ashfold, M.; Baletto, F.; Baumberg, J.; Christopher, P.; Cortés, E.; de Nijs, B.; Diaz Fernandez, Y.; Gargiulo, J.; Gawinkowski, S.; et al. Dynamics of Hot Electron Generation in Metallic Nanostructures: General Discussion. *Faraday Discuss.* **2019**, *214*, 123−146.

(10) Sivan, Y.; Baraban, J.; Un, I. W.; Dubi, Y. Comment on "Quantifying Hot Carrier and Thermal Contributions in Plasmonic Photocatalysis. *Science* **2019**, *364*, No. eaaw9367.

(11) Zhang, X.; Li, X.; Reish, M. E.; Zhang, D.; Su, N. Q.; Gutiérrez, Y.; Moreno, F.; Yang, W.; Everitt, H. O.; Liu, J. Plasmon-enhanced Catalysis: Distinguishing Thermal and Nonthermal Effects. *Nano Lett.* **2018**, *18*, 1714−1723.

(12) Yu, Y.; Sundaresan, V.; Willets, K. A. Hot Carriers Versus Thermal Effects: Resolving the Enhancement Mechanisms for Plasmon-mediated Photoelectrochemical Reactions. *J. Phys. Chem. C* **2018**, *122*, 5040−5048.

(13) Kamarudheen, R.; Castellanos, G. W.; Kamp, L. P. J.; Clercx, H. J. H.; Baldi, A. Quantifying Photothermal and Hot Charge Carrier Effects in Plasmon-driven Nanoparticle Syntheses. *ACS Nano* **2018**, *12*, 8447−8455.

(14) Kamarudheen, R.; Aalbers, G. J. W.; Hamans, R. F.; Kamp, L. P. J.; Baldi, A. Distinguishing Among All Possible Activation Mechanisms of a Plasmon-Driven Chemical Reaction. *ACS Energy Letters* **2020**, *5*, 2605−2613.

(15) Zhou, X.; Xu, W.; Liu, G.; Panda, D.; Chen, P. Size-dependent Catalytic Activity and Dynamics of Gold Nanoparticles at the Single-molecule Level. *J. Am. Chem. Soc.* **2010**, *132*, 138−146.

(16) Ye, X.; Zheng, C.; Chen, J.; Gao, Y.; Murray, C. B. Using Binary Surfactant Mixtures to Simultaneously Improve the Dimensional Tunability and Monodispersity in the Seeded Growth of Gold Nanorods. *Nano Lett.* **2013**, *13*, 765−771.

(17) Burda, C.; Chen, X.; Narayanan, R.; El-Sayed, M. A. Chemistry and Properties of Nanocrystals of Different Shapes. *Chem. Rev.* **2005**, *105*, 1025−1102.

(18) Hansen, P. L.; Wagner, J. B.; Helveg, S.; Rostrup-Nielsen, J. R.; Clausen, B. S.; Topsøe, H. Atom-resolved Imaging of Dynamic Shape Changes in Supported Copper Nanocrystals. *Science* **2002**, *295*, 2053−2055.

(19) Zhang, Y.; Lucas, J. M.; Song, P.; Beberwyck, B.; Fu, Q.; Xu, W.; Alivisatos, A. P. Superresolution Fluorescence Mapping of Single-nanoparticle Catalysts Reveals Spatiotemporal Variations in Surface Reactivity. *Proc. Natl. Acad. Sci. U. S. A.* **2015**, *112*, 8959−8964.

(20) Zugic, B.; Wang, L.; Heine, C.; Zakharov, D. N.; Lechner, B. A.; Stach, E. A.; Biener, J.; Salmeron, M.; Madix, R. J.; Friend, C. M. Dynamic Restructuring Drives Catalytic Activity on Nanoporous Gold−silver Alloy Catalysts. *Nat. Mater.* **2017**, *16*, 558−564.

(21) Xu, W.; Kong, J. S.; Yeh, Y.-T. E.; Chen, P. Single-molecule Nanocatalysis Reveals Heterogeneous Reaction Pathways and Catalytic Dynamics. *Nat. Mater.* **2008**, *7*, 992−996.
(22) Buurmans, I. L.; Weckhuysen, B. M. Heterogeneities of Individual Catalyst Particles in Space and Time As Monitored by Spectroscopy. *Nat. Chem.* **2012**, *4*, 873.
(23) Cortés, E.; Xie, W.; Cambiasso, J.; Jermyn, A. S.; Sundararaman, R.; Narang, P.; Schlücker, S.; Maier, S. A. Plasmonic Hot Electron Transport Drives Nano-localized Chemistry. *Nat. Commun.* **2017**, *8*, 1−10.
(24) Hamans, R. F.; Kamarudheen, R.; Baldi, A. Single Particle Approaches to Plasmon-Driven Catalysis. *Nanomaterials* **2020**, *10*, 2377.
(25) Zou, N.; Chen, G.; Mao, X.; Shen, H.; Choudhary, E.; Zhou, X.; Chen, P. Imaging Catalytic Hotspots on Single Plasmonic Nanostructures Via Correlated Super-resolution and Electron Microscopy. *ACS Nano* **2018**, *12*, 5570−5579.
(26) Li, W.; Miao, J.; Peng, T.; Lv, H.; Wang, J.-G.; Li, K.; Zhu, Y.; Li, D. Single-molecular Catalysis Identifying Activation Energy of the Intermediate Product and Rate-limiting Step in Plasmonic Photocatalysis. *Nano Lett.* **2020**, *20*, 2507−2513.
(27) Brown, A. M.; Sundararaman, R.; Narang, P.; Goddard, W. A., III; Atwater, H. A. Nonradiative Plasmon Decay and Hot Carrier Dynamics: Effects of Phonons, Surfaces, and Geometry. *ACS Nano* **2016**, *10*, 957−966.
(28) Zhang, Y.; Yam, C.; Schatz, G. C. Fundamental Limitations to Plasmonic Hot-carrier Solar Cells. *J. Phys. Chem. Lett.* **2016**, *7*, 1852−1858.
(29) Wu, K.; Chen, J.; McBride, J. R.; Lian, T. Efficient Hot-electron Transfer by a Plasmon-induced Interfacial Charge-transfer Transition. *Science* **2015**, *349*, 632−635.
(30) Boerigter, C.; Campana, R.; Morabito, M.; Linic, S. Evidence and Implications of Direct Charge Excitation as the Dominant Mechanism in Plasmon-mediated Photocatalysis. *Nat. Commun.* **2016**, *7*, 1−9.
(31) Boerigter, C.; Aslam, U.; Linic, S. Mechanism of Charge Transfer from Plasmonic Nanostructures to Chemically Attached Materials. *ACS Nano* **2016**, *10*, 6108−6115.
(32) Seemala, B.; Therrien, A. J.; Lou, M.; Li, K.; Finzel, J. P.; Qi, J.; Nordlander, P.; Christopher, P. Plasmon-mediated Catalytic O2 Dissociation on Ag Nanostructures: Hot Electrons or Near Fields? *ACS Energy Letters* **2019**, *4*, 1803−1809.
(33) Chen, G.; Zou, N.; Chen, B.; Sambur, J. B.; Choudhary, E.; Chen, P. Bimetallic Effect of Single Nanocatalysts Visualized by Super-resolution Catalysis Imaging. *ACS Cent. Sci.* **2017**, *3*, 1189−1197.
(34) Wertz, E.; Isaacoff, B. P.; Flynn, J. D.; Biteen, J. S. Single-molecule Super-resolution Microscopy Reveals How Light Couples to a Plasmonic Nanoantenna on the Nanometer Scale. *Nano Lett.* **2015**, *15*, 2662−2670.
(35) Wertz, E. A.; Isaacoff, B. P.; Biteen, J. S. Wavelength-dependent Super-resolution Images of Dye Molecules Coupled to Plasmonic Nanotriangles. *ACS Photonics* **2016**, *3*, 1733−1740.
(36) Taylor, A.; Verhoef, R.; Beuwer, M.; Wang, Y.; Zijlstra, P. All-optical Imaging of Gold Nanoparticle Geometry Using Super-resolution Microscopy. *J. Phys. Chem. C* **2018**, *122*, 2336−2342.
(37) Chattopadhyay, S.; Biteen, J. S. Super-resolution Characterization of Heterogeneous Light-matter Interactions between Single Dye Molecules and Plasmonic Nanoparticles. *Anal. Chem.* **2021**, *93*, 430−444.
(38) Gorelikov, I.; Matsuura, N. Single-step Coating of Mesoporous Silica on Cetyltrimethyl Ammonium Bromide-capped Nanoparticles. *Nano Lett.* **2008**, *8*, 369−373.
(39) van der Hoeven, J. E. S. *Gold Based Nanorods: Tuning the Structure for Catalysis and Sensing;* Utrecht University: Utrecht, The Netherlands, 2019.
(40) Zhou, X.; Andoy, N. M.; Liu, G.; Choudhary, E.; Han, K.-S.; Shen, H.; Chen, P. Quantitative Super-resolution Imaging Uncovers Reactivity Patterns on Single Nanocatalysts. *Nat. Nanotechnol.* **2012**, *7*, 237.
(41) Thompson, R. E.; Larson, D. R.; Webb, W. W. Precise Nanometer Localization Analysis for Individual Fluorescent Probes. *Biophys. J.* **2002**, *82*, 2775−2783.
(42) Ovesnỳ, M.; Křížek, P.; Borkovec, J.; Švindrych, Z.; Hagen, G. M. ThunderSTORM: A Comprehensive ImageJ Plug-in for PALM and STORM Data Analysis and Super-resolution Imaging. *Bioinformatics* **2014**, *30*, 2389−2390.
(43) Hamans, R. F.; Parente, M.; Castellanos, G. W.; Ramezani, M.; Gómez Rivas, J.; Baldi, A. Super-resolution Mapping of Enhanced Emission by Collective Plasmonic Resonances. *ACS Nano* **2019**, *13*, 4514−4521.
(44) Yorulmaz, M.; Khatua, S.; Zijlstra, P.; Gaiduk, A.; Orrit, M. Luminescence Quantum Yield of Single Gold Nanorods. *Nano Lett.* **2012**, *12*, 4385−4391.
(45) Zou, N.; Zhou, X.; Chen, G.; Andoy, N. M.; Jung, W.; Liu, G.; Chen, P. Cooperative Communication Within and Between Single Nanocatalysts. *Nat. Chem.* **2018**, *10*, 607−614.
(46) Alexander, G. B.; Heston, W.; Iler, R. K. The Solubility of Amorphous Silica in Water. *J. Phys. Chem.* **1954**, *58*, 453−455.
(47) Chau, Y.-F.; Chen, M. W.; Tsai, D. P. Three-dimensional Analysis of Surface Plasmon Resonance Modes on a Gold Nanorod. *Appl. Opt.* **2009**, *48*, 617−622.

https://dx.doi.org/10.1021/acs.nanolett.0c04837
Nano Lett. 2021, 21, 2149−2155